Modelling the thermal-hydro-mechanical behaviour of unsaturated soils with a high degree of saturation using extended precise integration method

Lujun Wang[1, *], Peter John Cleall[2], Bin Zhu[3], Yunmin Chen[4]

1. Associate Professor (* corresponding author), Center for Hypergravity Experimental and Interdisciplinary Research, MOE Key Laboratory of Soft Soils and Geoenvironmental Engineering, Zhejiang University, Hangzhou, 310058, China. E-mail: lujunwang@zju.edu.cn. ORCID: 0000-0002-0384-4941.

2. Professor, Geoenvironmental Research Centre, School of Engineering, Cardiff University, Cardiff CF24 3AA, U.K. E-mail: cleall@cardiff.ac.uk. ORCID: 0000-0002-4005-5319

3. Professor, Center for Hypergravity Experimental and Interdisciplinary Research, MOE Key Laboratory of Soft Soils and Geoenvironmental Engineering, Zhejiang University, Hangzhou, 310058, China. E-mail: binzhu@zju.edu.cn.

4. Professor, Center for Hypergravity Experimental and Interdisciplinary Research, MOE Key Laboratory of Soft Soils and Geoenvironmental Engineering, Zhejiang University, Hangzhou, 310058, China. E-mail: chenyunmin@zju.edu.cn.

Abstract

Unsaturated soils with a high degree of saturation (HDS) are commonly encountered in marine and lacustrine sediments. In these soils, the gas phase generally exists in the state of discrete bubbles, which is sensitive to stress and temperature changes and can dramatically change the soil's engineering properties. This paper explores the thermal-induced behaviour of HDS soils using an efficient extended precise integration method (XPIM). Biot poroelasticity theory, extended to include thermal effects and compressibility of gas-water mixture, is employed to analyze the soil behaviour under non-isothermal condition. Based on Laplace-Fourier transform and Taylor series expansion, such problems can be solved by XPIM. The robustness of XPIM was confirmed by comparing the present results with analytical solutions and test data. Extensive parametric studies are undertaken to examine both the effects of soil grain thermal expansion and anisotropic permeability on soil behaviour, and temperature effects on degree of saturation (S_r). The thermal-induced variations in S_r are more pronounced with lower initial values (e.g. 90% compared to 99%). These quantitative results demonstrate the benefits of the proposed method, which proves to be extremely efficient and several orders more precise than conventional numerical approaches, with its precision limited only by the computational effort used.

Keywords: thermal-hydro-mechanical coupling, unsaturated soil, degree of saturation, excess pore pressure, anisotropic permeability, extended precise integration method.

1 Introduction

Free and dissolved gases, normally produced biogenically or thermogenically, are encountered in many soils, most commonly in marine environments like offshore sediments and hydrate-bearing sediments (Fredlund and Rahardjo 1993; Fleischer et al. 2001; Waite et al. 2009; Hong et al. 2020). Many studies of unsaturated soils assume that two continuous fluid phases are present within the pore structure (Fredlund and Rahardjo 1993; Mihalache and Buscarnera 2016). However microscopic studies have revealed that at higher degrees of saturation the gas phase can be, as illustrated in Fig. 1, in a discontinuous state, forming discrete bubbles or voids within a continuous water phase (Sills et al. 1991; Mihalache and Buscarnera 2016). Such quasi-saturated soils (QSS), where the liquid phase is continuous and the gas phase is in the form of discrete bubbles wholly within in the liquid phase (Grozic *et al.* 1999; Bear and Cheng 2010), usually have high degrees of saturation (HDS) (85%≤ S_r ≤100%) and are relevant to numerous engineering applications (Faybishenko 1995; Sakaguchi et al. 2005; Tarantino 2013). The presence of a gas phase significantly effects both consolidation processes and strength characteristics, with quasi-saturated soils reacting differently compared with saturated soils to environmental changes in load and temperature (Sills and Wheeler 1992; Amaratunga and Grozic 2009). On account of the complexity and uncertainty of hydro-mechanical properties, research into gas-charged sediments has gained great interest particularly in the context of environmental issues, gas hydate production and in turn for the planning of on- and offshore engineering operations (Sultan and Garziglia 2014; Hong et al. 2017). Some of the most prominent examples have been reported in ocean sediments, oil-sand deposits and gas-hydrate sediments (Fourie *et al.* 2001; Amaratunga and Grozic 2009).

In HDS soils, the pore water and bubbles behave as a ‘‘compressible fluid’’ flowing under pressure or temperature gradients, surface tension and therefore the difference between the gas and water tension appear to be unimportant (Chang and Duncan 1983; Okusa 1985; Chen 2004). Considering Boyle's Law and Henry’s Law, Fredlund (1976) formulated the compressibility and density equations for gas-water mixtures (GWM), and then, Pietruszczak and Pande (1996) modified the representation of the compressibility of GWM by considering the effect of surface tension. After that, consolidation problems of soils with compressible fluid and solid constituents were extensively studied (Rajapakse and Senjuntichai 1993; Yue et al. 1994; Lade and DE Boer 1997; Chen 2004; Rani et al. 2011).

Fig. 1

In the applications such as heated pipelines for offshore oil transportation, marine gas hydrate production, disposal of nuclear waste, sediment sampled from the deep seabed for laboratory testing at room temperature, and energy facilities with elevated temperatures (Waite et al. 2009; Rotta Loria and Laloui 2017; Li et al. 2018), heat energy is usually transferred to the soils resulting in significant

changes of soil temperature. Occluded gas bubbles in pores are very sensitive to temperature change. When temperature rises, the bubbles expand and both the processes of seepage and deformation are influenced accordingly, which can strongly affect the engineering characteristics of soils and make the hydro-mechanical coupling processes much more complicated. However, little research evidence on thermal-hydro-mechanical (THM) coupling behaviour of HDS soils is available, although the temperature influence on the hydro-mechanical behaviour and characteristics of bubbles in GWM has been highlighted in previous investigations (Sills et al. 1991; Fredlund and Rahardjo 1993; Sultan et al. 2012; Selvadurai and Najari 2017; Zhu et al. 2020). A number of relevant works have focused on the THM behaviour of saturated soils (Sultan et al. 2002; Cui et al. 2009; Selvadurai and Suvorov 2014; Ai and Wang, 2016) or unsaturated soils with continuous gas phase (Thomas et al. 2009; Zhu et al. 2020). Apart from a limited number of studies (Selvadurai and Najari 2017; Wang and Ai 2018) discussing the influence of pore fluid compressibility on THM responses, no research effort has been directed to explore the coupling effects of S_r, temperature and thermal expansion characteristics of soil grains on the behaviour of the HDS soils. In summary, considering the fact that the thermal expansion of gas bubbles is very sensitive to temperature change and can strongly affect the processes both of seepage and deformation, it is necessary to examine the thermal effects on the variation of degree of saturation and hydro-mechanical coupling behaviour of HDS unsaturated soils.

This paper presents a comprehensive investigation of the 3D coupling behaviour of heat conduction, seepage and deformation of HDS unsaturated soils with temperature dependent degree of saturation using an efficient extended precise integration method (XPIM). Firstly, Biot classical poroelasticity theory, extended to include thermal effects and compressibility of GWM, is developed. By employing Laplace and Fourier transforms, the complex partial differential equations (PDEs) in the physical domain can be reduced to ordinary differential equations (ODEs) in the transformed domain. Each typical soil layer is divided into 2^N layer-elements with identical thickness, and the relational matrices of ODEs at the surface and bottom of any layer-element can be expressed by Taylor series expansion. Thus, desired precision, limited only by the computer used, can be ideally reached. With the aid of the recurrence rule for combining two adjacent layer-elements, a typical soil layer is assembled after N iterations of this combination. The final solution can be further obtained by introducing the external loads and boundary conditions. The precise integraton method (PIM) (Zhong 2004; Zhong et al. 2004) proves to be suitable in solving the mixed boundary value problems with complicated governing equations, with no need to deduce the explicit expressions. Moreover, the dimensions of the corresponding matrices are relatively small and, even more importantly, invariable throughout the computation. With the inherent advantages of PIM, the present XPIM avoids the exponential overflow in numerical computation and its efficiency and accuracy can be guaranteed by employing optimized numerical inversion techniques. By combining the integral transform method and the PIM (Zhong 2004; Zhong et al. 2004), the present XPIM can solve more complex and range problems in the transformed

domain efficiently and accurately, as well as the problem with a general load applied at an arbitrary depth. The XPIM results were compared with an analytical solution (Chen 2004) and test data (Savvidou and Booker 1991) for verification purpose. Extensive parametric studies are then undertaken to explore both the effects of soil grain thermal expansion and anisotropic permeability on the soil behaviour, and temperature effects on degree of saturation.

2 Methodology

2.1 Coupled THM Formulations

A HDS unsaturated soil consists of solid skeleton, pore water, free gas, as well as dissolved gas, which is part of the water volume and shows significant effect on pore water compressibility (Fredlund 1976). In THM coupling analysis, the following assumptions are made (1) different phases are equally distributed in the control volume; (2) the water is continuous; (3) the gas phase embedded in water is in the form of small gas bubbles and dissolved gas (Pietruszczak and Pande 1996); (4) the three phases exhibit mechanical and thermal deformations, related to stresses and temperature increment applied to the phases. At any given point, all three phases are in thermal equilibrium; (5) the degree of saturation S_r, defined as water volume per void volume, is in the range of 85% and 100% (Tarantino 2013); (6) the strain, stress, and temperature increments are small, and the theory is quasi-static; (7) the water and gas dissolved in water are described as GWM (Fredlund and Rahardjo 1993); (8) the GWM flow follows Darcy's law and heat transfer follows Fourier's law. According to these assumptions, a three-dimensional (3D) XPIM model based on the following governing equations is developed for modelling the THM coupling behaviour of HDS

Equilibrium equation and constitutive equation

The equilibrium equation of the THM coupling problems neglecting the body forces in Cartesian coordinates takes the form

$$\nabla \cdot \boldsymbol{\sigma} = 0 \tag{1}$$

where $\boldsymbol{\sigma}$ denotes stress increments with respect to an initial condition accounting for the external load. ∇ denotes the gradient operator. Temperature increment induces volumetric deformation and, subsequently, the stress in the soil skeleton. Considering the volumetric thermal expansion, the constitutive equation governing the relationships between the total stress, strain, and temperature increment takes the form (Biot 1957; Selvadurai and Suvorov 2014; Wang *et al.* 2019a; Hong *et al.* 2021)

$$\boldsymbol{\sigma} = 2G\boldsymbol{\varepsilon} + \lambda\varepsilon_v\mathbf{I} + bS_{r0}u_w\mathbf{I} + bS_{a0}u_a\mathbf{I} - \beta_s KT\mathbf{I} \tag{2}$$

where G and $\lambda = \frac{2G\mu}{1-2\mu}$ denote, respectively, the shear modulus and Lamé coefficient, here μ is Poisson's ratio; $\boldsymbol{\varepsilon}$ is the strain tensor; β_s denotes the volumetric thermal expansion of solid matrix; S_{r0}

and S_{a0} denote the initial water saturation and gas saturation, respectively; u_w and u_a are pore water pressure and pore gas pressure, respectively; *T* denotes the temperature increment; $K = \frac{2G(1+\mu)}{3(1-2\mu)}$ denotes the bulk modulus of soil skeleton and $\mathbf{I}$ denotes the unit tensor; ε_v represents the volumetric strain with the expression

$$\varepsilon_v = \mathrm{tr}\boldsymbol{\varepsilon} \tag{3}$$

here tr denotes the trace of a given matrix. The effective stress, $\boldsymbol{\sigma}'$, is given by

$$\boldsymbol{\sigma}' = \boldsymbol{\sigma} - bS_{r0}u_w\mathbf{I} - bS_{a0}u_a\mathbf{I} \tag{4a}$$

Considering the fact that u_w in HDS soil is very close to u_a, and thus assuming that $u_w = u_a = u$ (Fredlund and Rahardjo 1993; Pietruszczak and Pande 1996), the sum of S_{r0} and S_{a0} equals to the unity, Eq. (4a) can be rewritten as

$$\boldsymbol{\sigma}' = \boldsymbol{\sigma} - bu\mathbf{I} \tag{4b}$$

The effective stress is often given as the difference between the total stress and the pore pressure, here *b* denotes the fraction of pore pressure that gives the effective stress, *u* denotes the pore pressure (EPP). The expressions of *b* have been presented by several literatures (Terzaghi 1936; Biot and Willis 1957; Skempton 1960; Schiffman 1970; Bishop 1973; Lade and Bore 1997; Chapuis 2004; Borja and Koliji 2009; Deng *et al.* 2011; Liang *et al.* 2017; Hong *et al.* 2021), as shown in Table 1. Table 1 indicates that there is no available expression of *b* valid for all classes of soils. The value of *b* = 1 corresponds to Terzaghi's original law (Terzaghi 1936), which assumes that the macroscopic compressibility of the soil skeleton is much higher than the intrinsic compressibility of the grain, and ignores the compressibility of pore water and gas. The suggestion of *b = n, where n is the porosity, is an intuitive proposition whose effect is to eliminate the pore pressure when n is zero (Terzaghi 1945; Biot 1955). Based on two-phase mixture theory, a rigorous evaluation of b has been developed by simulating a series of separate grains with interconnected contact points (Lade and De Bore 1997), this evaluation of b is suitable for dense sand. For the structure and directionality in HDS soft soils, the specific value of compressibility mainly depends upon the shapes and arrangements of the particles, rather than the intrinsic compressibility of soil grains C_{sg} (Mitchell and Soga 2005; Liang et al. 2017). In this case, the total stress $\Delta\sigma$ is supposed to be applied in two steps: a pore pressure Δu is firstly applied on both the pore water and skeleton, and then a load $(\Delta\sigma - \Delta u)$ is applied on the skeleton only. In the first step, Δu leads to stress increase both in the pore water and skeleton, and volumetric change $(C_{ssk}V\Delta u)$. In the second step, the volume change includes deformation due to sliding and rolling of the structure with a linear (Black and Lee 1973; Liang et al, 2017). In the two steps, the total volume change and the corresponding volume strain can be expressed as*

$$\Delta V = C_{ssk}V\Delta u + C_sV(\Delta\sigma - \Delta u) \tag{5a}$$

$$\varepsilon = \frac{\Delta V}{V} = C_s \Delta \sigma'$$

(5b)

from which

$$\Delta \sigma' = \Delta \sigma - (1 - \frac{C_{ssk}}{C_s}) \Delta u = \Delta \sigma - b \Delta u$$

(6)

here C_{ssk} is the compressibility of soil skeleton due to the total pressure change, C_s is the compressibility of soil as a whole, V denotes the initial volume of the soil element.

Table 1

Mass balance equations

Neglecting the body forces, the GWM flow in soils follows the generalized Darcy's law

$$\mathbf{q}_f = -\frac{1}{\gamma_w} \mathbf{c} \nabla u$$

(7a)

$$\mathbf{c} = \begin{bmatrix} c_h & 0 & 0 \\ 0 & c_h & 0 \\ 0 & 0 & c_v \end{bmatrix}$$

(7b)

where $\mathbf{q}_f$ is the advective (Darcy's) flux and γ_w denotes the pore mixture unit weight; $\mathbf{c}$ is the matrix of permeability coefficients; c_h and c_v denote the horizontal and vertical permeability, respectively. Owing to the long-term geological deposition process, natural soils often show strongly anisotropic fluid permeability (Scholes *et al.* 2007; Adams *et al.* 2013; Wongsaroj *et al.* 2013). The permeability anisotropy is commonly defined by the ratio r_c of the horizontal to vertical permeability, therefore

$$r_c = \frac{c_h}{c_v}$$

(7c)

For most natural clays and uniform mudrocks below seafloor, r_c increases from 1 to 4 (Scholes *et al.* 2007; Adams *et al.* 2013), and was reported to be greater than 10 in some regions (Arch and Maltman, 1990). c_v can be expressed as a function of porosity n (Chapuis and Aubertin 2003). Considering the reduced effective porosity due to the gas bubbles in HDS soils, the following expression can describes the saturation-dependent permeability based on the Kozeny-Carman model (Carman 1956)

$$c_v = \frac{1}{5S_g^2} \frac{(S_r n)^3}{(1 - S_r n)^2} = c_0 \frac{(S_r n)^3}{(1 - S_r n)^2}$$

(7d)

here $c_0 = \frac{1}{5S_g^2}$ is intrinsic permeability of soil, S_g denotes the specific surface area of soil grains (Sanzeni *et al*, 2013; Liang *et al.* 2017).

Based on the generalized Darcy's law, the flow Q_{fi} in the i-direction from time 0 to t is

$$Q_{fi} = \int_0^t q_{fi} \mathrm{d}t$$

(8)

Considering the temperature effects on the physical properties of water, and assuming that the deformation rates of the soil skeleton and the movement rate of water through the pore space do not generate heat, the non-linear PDEs governing the behavior of HDS soils can be given by (Selvadurai and Najari 2017; Wang *et al.* 2019a)

$$\frac{1}{\gamma_w}\left[c_h\left(\frac{\partial^2 u}{\partial x^2}+\frac{\partial^2 u}{\partial y^2}\right)+c_v\frac{\partial^2 u}{\partial z^2}\right]=b\frac{\partial \varepsilon_v}{\partial t}+S_c\frac{\partial u}{\partial t}-\beta_{ls}\frac{\partial T}{\partial t}$$

(9)

where

$$S_c=nC_{lg}+(b-n)C_{ssk}$$

(10a)

$$C_{lg}=S_rC_lB_l+(1-S_r+h_gS_r)C_gB_g$$

(10b)

$$\beta_{ls}=n\beta_l+(b-n)\beta_s$$

(10c)

in which C_{lg} is the compressibility of GWM, C_l and C_g are, respectively, the compressibility of water and gas; B_l and B_g are, respectively, the pore-water and pore-gas pressure coefficient for isotropic load, both of which are commonly supposed to be 1.0; ∇^2 is the Laplace operator, h_g denotes the coefficient of gas dissolved in water, which is the percentage of dissolved gas with respect to the water volume; β_l is the volumetric thermal expansion coefficient of water.

For non-isothermal condition, the behavior of the gas bubbles follows the ideal gas law

$$\frac{P^gV^g}{T^t}=mR$$

(11a)

where V^g is the volume of gas, P^g denotes the absolute pressure of gas bubble, T^t denotes the temperature in degrees Kelvin, m denotes the number of moles and R denotes the universal gas constant. Applying a derivative to Eq. (11a) produces (Selvadurai and Najari 2017)

$$P^g\mathrm{d}V^g+V^g\mathrm{d}P^g=mR\mathrm{d}T^t\Rightarrow C_g=\frac{-\mathrm{d}V^g/V^g}{\mathrm{d}P^g}=\frac{1}{P^g}-\frac{1\,\mathrm{d}T^t}{T^t\mathrm{d}P^g}$$

(11b)

According to the ideal gas law, the gas fraction (1-S_r) changes with the effects of pressure and temperature. Assuming that the total volume of the water and gas are constant ($V^l+V^g=V_0^l+V_0^g$), the expression of gas fraction during the THM process can be given by

$$\frac{P^gV^g}{T^t}=\frac{P_0^gV_0^g}{T_0^t},\ 1-S_r=\frac{V^g}{V^l+V^g}\Rightarrow 1-S_r=\frac{P_0^gT^t}{P^gT_0^tV^l+V^g}=\frac{P_0^gT^t}{P^gT_0^t}(1-S_{r0})$$

(11c)

The degree of saturation during the THM process can be rewritten as

$$S_r = 1 - \frac{P_0^g T^t}{P^g T_0^t}(1 - S_{r0})$$

(11d)

where V_0^g denotes the initial volume of gas, P_0^g denotes the initial absolute gas pressure, T_0^t denotes the reference temperature and S_{r0} denotes the initial S_r.

Energy balance equations

For quasi–static THM coupling problems in HDS soils with relatively low permeability, it can be assumed that there exist few complete seepage channels and neither the pore fluid flow rates nor the deformation rates of the material bring about heat generation (Savvidou and Booker 1991; Selvadurai and Suvorov 2014). Thus, ignoring the convective terms, heat transfer in HDS soils is assumed to take place predominantly by heat conduction and be governed by Fourier's law

$$\mathbf{q}_T = -\mathbf{k}_T \nabla T$$

(12a)

$$\mathbf{k}_T = \begin{bmatrix} k_T & 0 & 0 \\ 0 & k_T & 0 \\ 0 & 0 & k_T \end{bmatrix}$$

(12b)

where $\mathbf{q}_T$ is the heat flux and k_T is the overall thermal conductivity of the soils. Considering the fact that variation of S_r has a little effect on k_T, here k_T can be expressed as the volume average of the phase thermal conductivities

$$k_T = nk_{Tf} + (1-n)k_{Ts}$$

(12c)

where k_{Tf} and k_{Ts} denote, respectively, the thermal conductivities of the liquid and solid phase.

For the time from 0 to t, the heat flow Q_{fi} in the i-direction can be obtained according to Fourier's law

$$Q_{Ti} = \int_0^t q_{Ti} \mathrm{d}t$$

(13)

Compared with thermal contributions, mechanical and seepage contributions to energy balance can be neglected in many engineering practices (Savvidou and Booker 1988). As of this, the net rate of energy to enter an element of the medium will be balanced by increases in the internal energy of pore water and solid matrix (Savvidou and Booker 1988; Ai and Wang 2016). Neglecting the convective terms and mechanical coupling leads to

$$-\nabla \mathbf{q}_T = C_{cls} \frac{\partial T}{\partial t}$$

(14a)

where C_{cls} is the overall heat capacity of the soil, which is defined as the volume average of the phase heat capacities

$$C_{cls} = (1-n)\rho_s C_{cs} + nS_r\rho_l C_{cl} + n(1-S_r)\rho_g C_{cg} \tag{14b}$$

in which ρ_s, ρ_l and ρ_g are, respectively, the densities of solid phase, water and gas; C_{cs}, C_{cl} and C_{cg} are, respectively, the specific heat capacities of solid phase, water and gas.

Combining Fourier's law Eq. (12a) and Eq. (14a) results in the conductive heat transfer equation

$$\frac{\partial T}{\partial t} = \frac{k_T}{C_{cls}}\nabla^2 T \tag{15}$$

2.2 Details of XPIM model

A standard matrix equation in the transformed domain

Owing to the difficulty in solving the previous PDEs directly, the integral transform method is utilized to transform the PDEs into ODEs. The Laplace-Fourier transform (LFT) of function $f(x, y, z, t)$ with respect to t, x and y, and its inversion are (Sneddon 1972)

$$\tilde{f}(\xi_x,\xi_y,z,s) = \frac{1}{4\pi^2}\int_0^\infty\int_{-\infty}^{\infty}\int_{-\infty}^{\infty} f(x,y,z,t)\times \mathrm{e}^{-st}\mathrm{e}^{-\mathrm{i}(x\xi_x + y\xi_y)}\mathrm{d}t\mathrm{d}x\mathrm{d}y \tag{16a}$$

$$f(x,y,z,t) = \frac{1}{2\pi\mathrm{i}}\int_{\gamma-\mathrm{i}\infty}^{\gamma+\mathrm{i}\infty}\int_{-\infty}^{\infty}\int_{-\infty}^{\infty}\tilde{f}(\xi_x,\xi_y,z,s)\times \mathrm{e}^{st}\mathrm{e}^{\mathrm{i}(x\xi_x + y\xi_y)}\mathrm{d}s\mathrm{d}\xi_x\mathrm{d}\xi_y \tag{16b}$$

where s, ξ_x and ξ_y are LFT parameters with respect to t, x and y, respectively.

Taking the application of LFT to Eqs. (1), (2), (8), (9), (13) and (15), the ODE in matrix form can be obtained

$$\frac{\partial}{\partial z}\begin{Bmatrix}\mathbf{V}(z)\\ \mathbf{U}(z)\end{Bmatrix} = \begin{bmatrix}\mathbf{\Phi}_1 & \mathbf{\Phi}_2\\ \mathbf{\Phi}_3 & \mathbf{\Phi}_4\end{bmatrix}\cdot\begin{Bmatrix}\mathbf{V}(z)\\ \mathbf{U}(z)\end{Bmatrix} \tag{17}$$

where $\mathbf{V}(z) = [\mathrm{i}\tilde{\sigma}_{xz}, \mathrm{i}\tilde{\sigma}_{yz}, \tilde{\sigma}_z, \tilde{u}, \tilde{T}]^{\mathrm{T}}$, $\mathbf{U}(z) = [\mathrm{i}\tilde{u}_x, \mathrm{i}\tilde{u}_y, \tilde{u}_z, \tilde{Q}_{fv}, \tilde{Q}_{Tv}]^{\mathrm{T}}$, $\mathbf{\Phi}_i$ (i = 1-4), denoted matrices of order 5 × 5, are listed in Appendix A.

Combination of adjacent layer-elements

The standard matrix Eq. (17) establishes the relationship of the state variables and their partial derivatives with respect to z. To solve this matrix equation, PIM (Zhong 2004; Zhong *et al.* 2004) is employed and extended in this study. A natural layered soil system, consists of N_0 layers, is investigated, as shown in Fig. 2. For a layer with thickness η, the layer is discretized into 2^N identical layer-elements with a thickness of $\ell = \eta/2^N$. A result with acceptable error range can be achieved when either ℓ is small enough or N is big enough; N = 20 is recommended by Zhong (2004) and is chosen here. To establish the relationship between the relational matrix of interlevel state vector and ODE of Eq. (17), the dual vectors **V** and **U** are introduced. For a layer-element [z_a, z_b], the intrinsic relation between the state variables on the top and bottom, corresponding to **V**(z) and **U**(z) in Eq. (17), can be

established via relation matrices (Zhong, *et al.* 2004)

$$\begin{Bmatrix}\mathbf{U}_a\\ \mathbf{V}_b\end{Bmatrix}=\begin{bmatrix}\mathbf{E} & \mathbf{Q}\\ -\mathbf{G} & \mathbf{F}\end{bmatrix}\cdot\begin{Bmatrix}\mathbf{U}_b\\ \mathbf{V}_a\end{Bmatrix} \tag{18a}$$

where **E**, **F**, **G** and **Q** denote relational matrices. For the layer-element with thickness ℓ, the relational matrices can be obtained by Taylor series expansion with ℓ and the matrices $\mathbf{\Phi}_i$ (i = 1-4) in Eq. (17) (Zhong *et al.* 2004; Wang *et al.* 2019b)

$$\mathbf{E}(\ell)\approx\mathbf{I}+\sum_{i=1}^{\mathrm{M}}\mathbf{e}_i\ell^i \quad , \quad \mathbf{Q}(\ell)\approx\sum_{i=1}^{\mathrm{M}}\mathcal{L}_i\ell^i, \tag{18b}$$

$$\mathbf{G}(\ell)\approx\sum_{i=1}^{\mathrm{M}}\mathbf{g}_i\ell^i \quad , \quad \mathbf{F}(\ell)\approx\mathbf{I}+\sum_{i=1}^{\mathrm{M}}\mathbf{f}_i\ell^i, \tag{18c}$$

where $\mathbf{e}_i$, $\mathcal{L}_i$, $\mathbf{g}_i$ and $\mathbf{f}_i$ (i = 1-M) are provided in Appendix B, M is the highest order in Taylor series expansion and M = 4 here.

For any two adjacent layer-elements 1 [z_a, z_b] and 2 [z_b, z_c], as shown in Fig. 3, the state vectors at the interface can be given as

$$\begin{Bmatrix}\mathbf{U}_a\\ \mathbf{V}_b\end{Bmatrix}=\begin{bmatrix}\mathbf{E}_1 & \mathbf{Q}_1\\ -\mathbf{G}_1 & \mathbf{F}_1\end{bmatrix}\cdot\begin{Bmatrix}\mathbf{U}_b\\ \mathbf{V}_a\end{Bmatrix} \quad \text{, for layer-element 1} \tag{19a}$$

$$\begin{Bmatrix}\mathbf{U}_b\\ \mathbf{V}_c\end{Bmatrix}=\begin{bmatrix}\mathbf{E}_2 & \mathbf{Q}_2\\ -\mathbf{G}_2 & \mathbf{F}_2\end{bmatrix}\cdot\begin{Bmatrix}\mathbf{U}_c\\ \mathbf{V}_b\end{Bmatrix} \quad \text{, for layer-element 2} \tag{19b}$$

By combining Eqs. (19a) and (19b), the relation between the state vectors at the top and bottom of a new combined layer-element A can be acquired

$$\begin{Bmatrix}\mathbf{U}_a\\ \mathbf{V}_c\end{Bmatrix}=\begin{bmatrix}\mathbf{E}_3 & \mathbf{Q}_3\\ -\mathbf{G}_3 & \mathbf{F}_3\end{bmatrix}\cdot\begin{Bmatrix}\mathbf{U}_c\\ \mathbf{V}_a\end{Bmatrix} \quad \text{, for layer-element A} \tag{20}$$

where

$$\mathbf{E}_3=\mathbf{E}_1(\mathbf{I}+\mathbf{Q}_2\mathbf{G}_1)^{-1}\mathbf{E}_2 \quad , \quad \mathbf{Q}_3=\mathbf{Q}_1+\mathbf{E}_1(\mathbf{Q}_2^{-1}+\mathbf{G}_1)^{-1}\mathbf{F}_1 \tag{21a}$$

$$\mathbf{G}_3=\mathbf{G}_2+\mathbf{F}_2(\mathbf{G}_1^{-1}+\mathbf{Q}_2)^{-1}\mathbf{E}_2 \quad , \quad \mathbf{F}_3=\mathbf{F}_2(\mathbf{I}+\mathbf{G}_1\mathbf{Q}_2)^{-1}\mathbf{F}_1 \tag{21b}$$

From the derivation process of Eq. (20), it shows that the combination is irrelevant with the order of elimination and combination; hence, it can be used as a recurrence rule for two adjacent layer-element combination. After repeating the process for *N* times, the relationship of the state vectors at the upper and lower surfaces of a natural layer is captured.

Fig. 2

Fig. 3

Solutions for XPIM model

For a multilayered soil system as illustrated in Fig. 2, three units can be formed from the N_0 layers according to the depths of load plane z_p and field point plane z_f (Wang *et al.* 2019a). Taking the application of Eq. (20) to the adjacent layer-elements and natural layers, the relational matrices of the three units can be obtained. Considering the relationship between z_p and z_f, three cases need to be discussed. When $z_p < z_f$

$$\begin{Bmatrix} \mathbf{U}_0 \\ \mathbf{V}_p^- \end{Bmatrix} = \begin{bmatrix} \hat{\mathbf{E}}_1 & \hat{\mathbf{Q}}_1 \\ -\hat{\mathbf{G}}_1 & \hat{\mathbf{F}}_1 \end{bmatrix} \cdot \begin{Bmatrix} \mathbf{U}_p^- \\ \mathbf{V}_0 \end{Bmatrix}$$

, for unit 1 (22a)

$$\begin{Bmatrix} \mathbf{U}_p^+ \\ \mathbf{V}_f \end{Bmatrix} = \begin{bmatrix} \hat{\mathbf{E}}_2 & \hat{\mathbf{Q}}_2 \\ -\hat{\mathbf{G}}_2 & \hat{\mathbf{F}}_2 \end{bmatrix} \cdot \begin{Bmatrix} \mathbf{U}_f \\ \mathbf{V}_p^+ \end{Bmatrix}$$

, for unit 2 (22b)

$$\begin{Bmatrix} \mathbf{U}_f \\ \mathbf{V}_{N_0} \end{Bmatrix} = \begin{bmatrix} \hat{\mathbf{E}}_3 & \hat{\mathbf{Q}}_3 \\ -\hat{\mathbf{G}}_3 & \hat{\mathbf{F}}_3 \end{bmatrix} \cdot \begin{Bmatrix} \mathbf{U}_{N_0} \\ \mathbf{V}_f \end{Bmatrix}$$

, for unit 3 (22c)

where $\mathbf{V}_p^-$, $\mathbf{U}_p^-$, $\mathbf{V}_p^+$, and $\mathbf{U}_p^+$ denote the generalized stresses and displacement variables at upper and lower surface of z_p, in which the intrinsic relationship $\mathbf{V}_p^+ = \mathbf{V}_p^- - \mathbf{P}_V$ and $\mathbf{U}_p^+ = \mathbf{U}_p^- - \mathbf{P}_U$ can be obtained when the external load $\mathbf{P}_V$ and dislocation $\mathbf{P}_U$ are applied.

Combining (22a), (22b) and (22c) and eliminating the state vectors at interface z_p, solutions for state vectors at interface z_f are obtained

$$\mathbf{V}_f = \left(\mathbf{I} + \hat{\mathbf{G}}_{12}\hat{\mathbf{Q}}_3\right)^{-1}\left(\hat{\mathbf{F}}_{12}\mathbf{V}_0 - \hat{\mathbf{G}}_{12}\hat{\mathbf{E}}_3\mathbf{U}_{N_0} - \hat{\mathbf{H}}_1\mathbf{P}_V - \hat{\mathbf{L}}_1\mathbf{P}_U\right)$$

(23a)

$$\mathbf{U}_f = \hat{\mathbf{Q}}_3\left[\left(\mathbf{I} + \hat{\mathbf{G}}_{12}\hat{\mathbf{Q}}_3\right)^{-1}\left(\hat{\mathbf{F}}_{12}\mathbf{V}_0 - \hat{\mathbf{G}}_{12}\hat{\mathbf{E}}_3\mathbf{U}_{N_0} - \hat{\mathbf{H}}_1\mathbf{P}_V - \hat{\mathbf{L}}_1\mathbf{P}_U\right)\right] + \hat{\mathbf{E}}_3\mathbf{U}_{N_0}$$

(23b)

where $\hat{\mathbf{F}}_{12}$, $\hat{\mathbf{E}}_{12}$, $\hat{\mathbf{G}}_{12}$, $\hat{\mathbf{Q}}_{12}$, $\hat{\mathbf{H}}_1$, $\hat{\mathbf{H}}_2$, $\hat{\mathbf{L}}_1$ and $\hat{\mathbf{L}}_2$ are constant matrices provided in Appendix C.

For $z_p > z_f$ case, the state vectors can be obtained in a similar process

$$\mathbf{V}_p = \hat{\mathbf{F}}_1\mathbf{V}_0 - \hat{\mathbf{G}}_1\left[\left(\mathbf{I} + \hat{\mathbf{Q}}_{23}\hat{\mathbf{G}}_1\right)^{-1}\left(\hat{\mathbf{Q}}_{23}\hat{\mathbf{F}}_1\mathbf{V}_0 - \hat{\mathbf{E}}_{23}\mathbf{U}_{N_0} - \hat{\mathbf{H}}_4\mathbf{P}_V + \hat{\mathbf{L}}_4\mathbf{P}_U\right)\right]$$

(24a)

$$\mathbf{U}_p = \left(\mathbf{I} + \hat{\mathbf{Q}}_{23}\hat{\mathbf{G}}_1\right)^{-1}\left(\hat{\mathbf{Q}}_{23}\hat{\mathbf{F}}_1\mathbf{V}_0 - \hat{\mathbf{E}}_{23}\mathbf{U}_{N_0} - \hat{\mathbf{H}}_4\mathbf{P}_V + \hat{\mathbf{L}}_4\mathbf{P}_U\right)$$

(24b)

where $\hat{\mathbf{Q}}_{23}$, $\hat{\mathbf{E}}_{23}$, $\hat{\mathbf{H}}_4$ and $\hat{\mathbf{L}}_4$ have the same expressions as $\hat{\mathbf{Q}}_{12}$, $\hat{\mathbf{E}}_{12}$, $\hat{\mathbf{H}}_4$ and $\hat{\mathbf{L}}_4$ in Eq. (23) provided that subscripts 2, 3, and 4 are substituted with 1, 2 and 2 sequentially.

Furthermore, for the special cases that $z_p = z_f$, $z_p = 0$ or $z_f = 0$, the thickness of special unit is 0, and previous results are still valid by setting the corresponding matrices **E**, **F**, **G**, **Q** as **I**, **I**, **0**, **0**, respectively.

Following the previous procedures, the solutions for pore pressure, stress, displacement and temperature are captured in the transformed domain. Then, the fixed Talbot approach (Abate and Valkó 2004), provided in Appendix D, for the Laplace transform inverse and the fractional Fourier transform (FRFT) approach (Bailey and Swarztrauber 1994), provided in Appendix E, for the Fourier transform inverse are utilized to obtain the actual solutions. The detailed operation procedure of XPIM is shown in Fig. 4.

Fig. 4 Overall scheme of the XPIM

2.3 Verification and validation against analytical and experimental results

The proposed model is compared with results from analytical solutions and experimental tests to provide verification and validation in terms of the hydro-mechanical (HM) behaviour to surface mechanical load and the THM behaviour to surface temperature change.

(1) HM behaviour subjected to surface mechanical load

An analytical solution obtained by the transfer matrix method (Chen 2004) for the problem of a circular uniform mechanical load q, with radius r_0, applied to the surface of a homogeneous soil layer with thickness $H = r_0$ is considered here. To reduce the unsaturated soil model with anisotropic permeability into an isotropic model, the permeability ratio r_c in Eq. (7c) is set as 1. For initial degrees of saturation S_r = 95.5%, 98.65%, 99.55% and 99.999% are chosen, and a Poisson's ratio of 0.25 is adopted. The time factor τ was defined as $\tau = c_v \mu t / r_0^2$ and results for a value of τ = 0.001 are considered in this example. Fig. 5 shows the EPP distribution against depth for different values of S_r, as attained by the analytical solution of Chen (2004), indicating that for decreasing values of S_r the excess pressure dissipates faster. The XPIM results agree well with those obtained by the analytical solution of Chen (2004). Moreover, the XPIM has the advantage that it is suitable to solve more complex THM coupling problems of layered saturated or HDS unsaturated soils, as it does not need to capture the explicit expressions of the solution and imposes no restriction on the number of layers and layer thickness.

Fig. 5

(2) THM behavior subjected to surface temperature change

The previous case concentrates on the mechanical load-induced HM behaviour of unsaturated soil with different values of S_r and is thus limited to poroelastic behaviour under isothermal conditions. Here a series of tests carried out by Savvidou and Booker (1991), where the THM coupling behaviour of

saturated soil due to application of a temperature change to a circular region, with radius $r_{0,}$ on the surface of a soil mass was considered, are investigated. The XPIM results and the test data by Savvidou and Booker (1991) are shown in Figs. 6(a) and 6(b). Poisson's ratio, Young's modulus, thermal diffusivity coefficient and consolidation coefficient were 0.25, 6000 kN/m^2, 3.5×10^3 cm^2/s and 10^3 cm^2/s respectively. The normalized parameters are defined as illustrated in Figs. 6(a) and 6(b). Reasonably good agreement of temperature variation at τ =0.3, 1.0 and EPP at τ = 0.3, 1.0, 3.0 can be captured between the XPIM and test results. The test data differed slightly from the XPIM results when τ = 0.1, which could be due to the small temperature change in a relatively short time, but the trends were the same. Generally, the present results show a good match with the test data.

Fig. 6

3 Results and discussion

A detailed parametric investigation is presented in this section to examine the influence of key factors, including thermal expansion characteristics of soil grains (β_l/β_s), initial degree of saturation (S_{rini}), temperature-dependent saturation and anisotropic permeability (c_h/c_v), on the behaviour of HDS soils. A temperature change $T(r)$ is applied to a circular region, with radius r_0 and uniform distributed thermal load 1 ℃/m^2, on the surface of the soil mass, as shown in Fig. 7. Poisson's ratio, Young's modulus, thermal diffusivity coefficient, consolidation coefficient and thermal consolidation coefficient of the soil are 0.25, 6000 kN/m^2, 3.5×10^3 cm^2/s, 10^3 cm^2/s and 0.33 respectively. $c^* = c_v/[\gamma_w(\lambda + 2G)]$ and $\tau = \kappa t/r_0^2$. The default (baseline) parameters along with values analyzed in the parametric investigation are provided in Table 2.

Fig. 7

Table 2

3.1 Effects of thermal expansion characteristics of soil grains

Fig. 8

Fig. 9

Figures 8 and 9 illustrate the effect of thermal expansion characteristics (β_l/β_s) of soil grains on the temperature variation and EPP distribution at different τ, respectively. Five values of β_l/β_s, 1, 2, 5, 10 and 1000, are considered and the value of β_l is held constant. Fig. 8 shows that thermal expansion characteristic has little influence on the temperature variation, this mainly due to that the thermal-

induced expansion is relative small compared with the depth of the soil model. Initially (τ = 0.01), relatively high EPP are captured at points close to the surface (z/r_0 = 0.1) owing to the thermal expansion of pore water, whilst negative excess pore pressure is generated at 0.3 < z/r_0 < 2, which can be attributed to the freedom of the surface to heave in the initial stage of heating, as shown in Fig. 9, here $u_N = 2G\beta_s(1+\mu)T/3(1-2\mu)$. Similar behaviour has been reported by Savvidou and Booker (1991) in model tests. Considering progressively increasing values of β_l/β_s (from 1 to 1000)of negative pore pressure decreases from 1.18 to 0.26 at about z/r_0 = 0.5. As τ increases from 0.1 to 0.5, the absolute peak of negative pore pressure decreases and tends to zero. Owing to the fact that the thermal expansion of pore water (β_l) is larger than that of soil grain (β_s), a temperature increment brings about a rise in EPP.

3.2 Impact of variation of initial S_r

To understand the THM behaviour of HDS soils, it is necessary to examine the effect of temperature changes on the variation of S_r. Fig. 10 illustrates the transient development of S_r with different initial degrees of saturation S_{rini} (90% and 99%) at different depths due to temperature change. In the initial stages, S_r firstly decreases with time, which result from the fact that the pore gas is more sensitive to temperature changes compared with pore water. Following that, S_r increases with time and reaches a peak, which is due to the thermally induced expansion of pore water being dominant at this stage. Then with EPP dissipation, the pore gas expands and S_r decreases and stabilizes at a value lower than S_{rini}. As illustrated in Figs. 10(a) and 10(b), the S_r peak is relatively delayed and lower with an increase of z/r_0 as a result of heat transfer and dissipation. As z/r_0 increases from 0.1 to 1.2, S_r decreases from 0.915 to 0.897 at z/r_0 = 0.1 and from 0.905 to 0.899 at z/r_0 = 1.2 for S_{rini} = 90% case. It can be seen that temperature change has a noticeable effect on the development of *S*span style="font-family:Arial; font-size:6.67pt; font-style:italic; vertical-align:sub">r, especially close to the temperature load, e.g. the difference between the peak and stable values is about 2%.

Fig. 10

Figure 11 shows the variation of S_r with depth for different values of S_{rini} subjected to surface temperature change. It can be seen that the variation of S_r with depth has similar trends for different S_{rini} values and tends towards a steady state. A peak appears close to the surface of the soil, and then progressively decreases and moves away from the surface with time. It is worth noting that the thermal-induced S_r variation with lower S_{rini} (e.g. 90%) is more obvious than that of higher S_{rini} (e.g. 99%), especially in the region of z/r_0 < 2. The temperature change of the soil has a significant effect on

S_r, especially for soil with relative low S_{rini} (e.g. from 85% to 95%), due to higher number of temperature sensitive isolated gas bubbles being present.

Fig. 11

3.3 Effect of anisotropic permeability c_h/c_v

This section examines the effect of anisotropic permeability (c_h/c_v, = 0.1, 1, 10, 50 and 100) on the evolution of EPP at depth of z/r_0=0.2 and vertical surface displacement over time. Fig. 12(a) indicates that a larger c_h/c_v ratio, is correlated to an earlier and smaller peak EPP value. The initial increases in EPP are largely due to the thermal expansion of pore gas bubbles and water, the EPP then decreases to a steady state value owing to the dissipation of pore gas-water mixture. The c_h/c_v ratio haa noticeable effect on the peak EPP value, but negligible effect on the steady state value.

The evolution of vertical displacement is strongly affected by c_h/c_v ratio, as shown in Fig. 12(b). For relative small c_h/c_v ratios (e.g. 0.1, 1 and 10), the vertical displacement increases over time towards a peak value and then progressively reduces to the final value, owing to the coupled process in the thermal expansions of pore GWM and solid skeleton and then dissipation of EPP. The peak value of $u_z/u_{z\infty}$ decreases from 2.1 to 1.0 as the c_h/c_v ratio increases from 0.1 to 100. The absence of a peak for the c_h/c_v = 100 case indicates that the pore GWM seepage mainly relies on horizontal flow in this case and not the build up of EPP. It is also worth noting that whilst the c_h/c_v ratio has a noticeable effect on the vertical displacement peak value, it does not affect the long term value, which is determined by the thermal expansion of the solid skeleton.

Fig. 12

3.4 Time-dependent behaviour

This section examines the time-dependent development of EPP and vertical surface displacement with different initial S_{rini} and depth z/r_0 subjected to surface temperature change. Fig. 13(a) shows very similar trends of EPP evolution at a depth z/r_0 = 0.2 for different values of S_{rini}. Results from Fig. 13(b) illustrate that the evolution of EPP at different depths z/r_0 over time is similar. As z/r_0 increases from 0.1 to 1.5, the EPP peak value u/u_N decreases from 3.42 to 0.84, and the time needed to achieve the peak gradually increased, which is related to the progressive transfer of heat through the domain.

Fig. 13

Fig. 14

Fig. 14(a) indicates the variation of vertical surface displacement with different initial values of S_{rini} here $u_{z\infty}$ denotes the long term stable vertical surface displacement, at lower values of S_r (e.g. 90.0%) slightly larger peak values are seen due to the thermal expansion of gas bubbles. The difference between the peak values of S_{rini} = 99.999% case and S_{rini} = 90.0% case is about 7.8%. Fig. 14(b) shows that the development of vertical displacement at various depths, has similar trends and tend towards a stable value. Interestingly, a small settlement appears before reaching the peak for the points at the depth of z/r_0 = 0.5, 0.8, 1.2 and 1.5, owing to the coupling effects between the thermal stress of the upper soil and the EPP dissipation within the lower soil layers.

The above computation for 3D THM coupling problems at any point of a HDS soil system costs less than 130s CPU time on an Intel Core i9-10900 2.81-GHz personal computer environment, which is remarkably less than that using traditional numerical methods, such as FEM.

4 Conclusions

This paper presents a precise numerical investigation of the coupled heat conduction, seepage and deformation behaviour of HDS unsaturated soils using the XPIM. The present model can explore the behaviour of HDS unsaturated soils surrounding heated pipelines for offshore oil transportation, disposal of nuclear waste, and other energy facilities with elevated temperatures. The robustness of the model was verified by comparing the present results with analytical solutions (Chen 2004) and test data (Savvidou and Booker 1991). Extensive parametric investigations were then carried out to examine the effects of thermal expansion of the soil grain and anisotropic permeability on the soil behaviours, and to examine the temperature effect on degree of saturation. The results have identified the following findings.

(1) The present XPIM has a wide applicability in complex THM coupling problems of layered and unsaturated soils, since thre is no limitation to the number and thickness of the layers, and an explicit solution is not required. Furthermore, any desired accuracy can be captured and is limited only by the computation effort utilized, owing to its intrinsic advantages in the combination of the 2^N type approach and Taylor series expansion.

(2) At relatively early stages of surface heating, high EPPs are captured at points close to the surface owing to the thermal-induced expansion of pore GWM, and negative pore pressure is generated below this region, which could be attributed to the freedom of the surface to heave in the initial heating stages. Since the pore water thermal expansion (β_l) is greater than that of soil grain (β_s), a temperature change causes a rise in EPP. EPP peak values increase with increasing value of the ratio β_l/β_s however because of EPP dissipation, the difference in peak values decreases to zero over time, which

may lead to soil liquefaction and shear failure of pipelines.

(3) Temperature change has a strong influence on the variation of degree of saturation (S_r), especially for soil with relative low initial S_r (e.g. from 85% to 95%). S_r firstly decreases with time owing to the fact that the pore gas is more sensitive to temperature changes compared with pore water; following that, S_r increase with time and reaches a peak, which is probably due to the thermal-induced expansion of pore water becoming gradually more dominant. The thermal-induced variation of the soil with lower initial S_r (e.g. 90%) is more obvious than that with higher value (e.g. 99%), especially in regions close to the surface (e.g. $z/r_0 < 2$). Thus, the thermal-induced variation of S_r need to be predicted to ensure the safety of energy facilities.

(4) The anisotropic permeability ratio c_h/c_v has a noticeable impact on peak EPP values, with larger c_h/c_v ratios inducing earlier and smaller EPP peak value, however it has a negligible effect on the long term values. The vertical displacement of soil with small c_h/c_v ratios (e.g. from 0.1 to 50) first increases with time, reaches a peak before stabilizing, while that with relative large ratio (e.g. 100) increases with time and tends to be stable without any peak being reached. A lower S_r (90.0%) induces a relatively larger peak compared with the saturated (S_r = 99.999%) case, which is due to the thermal expansion of gas bubbles. S_r has some effects on the peak value and dissipation process of EPP, while has little effect at the initial and stable stages.

Acknowledgements

The authors gratefully acknowledge the National Natural Science Foundation of China (Nos. 52078458 and 51988101), Zhejiang Provincial Natural Science Foundation of China (Nos. LY21E080026 and LCD19E090001) and Programme of Introducing Talents of Discipline to Universities (No. B18047).

Appendix A: Matrices of $\boldsymbol{\Phi}_i \ (\boldsymbol{i = 1 - 4})$.

$$\boldsymbol{\Phi}_1 = \begin{bmatrix} 0 & 0 & a_2\xi_x & a_3\xi_x & a_4\xi_x \\ 0 & 0 & a_2\xi_y & a_3\xi_y & a_4\xi_y \\ -\xi_x & -\xi_y & 0 & 0 & 0 \\ 0 & 0 & 0 & 0 & 0 \\ 0 & 0 & 0 & 0 & 0 \end{bmatrix}, \quad \boldsymbol{\Phi}_2 = \begin{bmatrix} a_5\xi_x^2 + \frac{1}{a_1}\xi_y^2 & a_6\xi_x\xi_y & 0 & 0 & 0 \\ a_6\xi_x\xi_y & a_5\xi_y^2 + \frac{1}{a_1}\xi_x^2 & 0 & 0 & 0 \\ 0 & 0 & 0 & 0 & 0 \\ 0 & 0 & 0 & f_1 & 0 \\ 0 & 0 & 0 & 0 & f_3 \end{bmatrix},$$

$$\boldsymbol{\Phi}_3 = \begin{bmatrix} a_1 & 0 & 0 & 0 & 0 \\ 0 & a_1 & 0 & 0 & 0 \\ 0 & 0 & a_7 & -b_1 & b_2 \\ 0 & 0 & -b_1 & g_1 & g_2 \\ 0 & 0 & 0 & 0 & g_3 \end{bmatrix}, \quad \boldsymbol{\Phi}_4 = \begin{bmatrix} 0 & 0 & \xi_x & 0 & 0 \\ 0 & 0 & \xi_y & 0 & 0 \\ -a_2\xi_x & -a_2\xi_y & 0 & 0 & 0 \\ -a_3\xi_x & -a_3\xi_y & 0 & 0 & 0 \\ 0 & 0 & 0 & 0 & 0 \end{bmatrix};$$

here $a_1 = \frac{1}{G}$, $a_2 = \frac{\mu}{1-\mu}$, $a_3 = \frac{b(1-2\mu)}{1-\mu}$, $a_4 = -\frac{\beta_s K(1-2\mu)}{1-\mu}$, $a_5 = \frac{2G}{1-\mu}$, $a_6 = \frac{G(1+\mu)}{1-\mu}$, $a_7 = \frac{1}{\lambda+2G}$, $b_1 = a_7 b$, $b_2 = -\frac{1}{2}a_1 a_4$, $f_1 = -\frac{s\gamma_w}{c_v}$, $f_2 = -\frac{c_h}{s\gamma_w}$, $f_3 = -\frac{s}{k_T}$, $g_1 = a_7 b^2 - S_c + f_2\xi^2$, $g_2 = \beta_{ls} + b_2 b$, $g_3 = \frac{1}{f_3}\xi^2 - C_{cls}$.

Appendix B: Expressions of matrices $\mathbf{e}_i$, $\mathcal{L}_i$, $\mathbf{g}_i$ and $\mathbf{f}_i$ $(i = 1 - \mathrm{M})$.

$$\mathbf{e}_1 = -\boldsymbol{\Phi}_4 \quad , \mathbf{e}_k = \frac{1}{k}\left(\boldsymbol{\Phi}_3\mathbf{g}_{k-1} - \mathbf{e}_{k-1}\boldsymbol{\Phi}_4 + \sum_{m-1}^{k-2}\mathbf{e}_m\boldsymbol{\Phi}_3\mathbf{g}_{k-m-1}\right), \quad (k = 2, 3, \ldots, \mathrm{M}) \tag{B1}$$

$$\mathcal{L}_1 = -\boldsymbol{\Phi}_3 \quad , \mathcal{L}_k = -\frac{1}{k}\left(\boldsymbol{\Phi}_3\mathbf{f}_{k-1} + \mathbf{e}_{k-1}\boldsymbol{\Phi}_3 + \sum_{m-1}^{k-2}\mathbf{e}_m\boldsymbol{\Phi}_3\mathbf{f}_{k-m-1}\right), \quad (k = 2, 3, \ldots, \mathrm{M}) \tag{B2}$$

$$\mathbf{g}_1 = -\boldsymbol{\Phi}_2 \quad , \mathbf{g}_k = \frac{1}{k}\left(\boldsymbol{\Phi}_1\mathbf{g}_{k-1} - \mathbf{g}_{k-1}\boldsymbol{\Phi}_4 + \sum_{m-1}^{k-2}\mathbf{g}_m\boldsymbol{\Phi}_3\mathbf{g}_{k-m-1}\right), \quad (k = 2, 3, \ldots, \mathrm{M}) \tag{B3}$$

$$\mathbf{f}_1 = \boldsymbol{\Phi}_1 \quad , \mathbf{f}_k = \frac{1}{k}\left(\boldsymbol{\Phi}_1\mathbf{f}_{k-1} + \mathbf{g}_{k-1}\boldsymbol{\Phi}_3 + \sum_{m-1}^{k-2}\mathbf{g}_m\boldsymbol{\Phi}_3\mathbf{f}_{k-m-1}\right), \quad (k = 2, 3, \ldots, \mathrm{M}) \tag{B4}$$

Appendix C: Expressions of matrices $\hat{\mathbf{F}}_{12}$, $\hat{\mathbf{E}}_{12}$, $\hat{\mathbf{G}}_{12}$, $\hat{\mathbf{Q}}_{12}$, $\hat{\mathbf{H}}_1$, $\hat{\mathbf{H}}_2$, $\hat{\mathbf{L}}_1$ and $\hat{\mathbf{L}}_2$.

$$\hat{\mathbf{F}}_{12} = \hat{\mathbf{F}}_2\left(\mathbf{I} + \hat{\mathbf{G}}_1\hat{\mathbf{Q}}_2\right)^{-1}\hat{\mathbf{F}}_1 \quad , \hat{\mathbf{G}}_{12} = \hat{\mathbf{G}}_2 + \hat{\mathbf{F}}_2\left(\hat{\mathbf{G}}_1^{-1} + \hat{\mathbf{Q}}_2\right)^{-1}\hat{\mathbf{E}}_2 \tag{C1}$$

$$\hat{\mathbf{Q}}_{12} = \hat{\mathbf{Q}}_1 + \hat{\mathbf{E}}_1\left(\hat{\mathbf{G}}_1 + \hat{\mathbf{Q}}_2^{-1}\right)^{-1}\hat{\mathbf{F}}_1 \quad , \hat{\mathbf{E}}_{12} = \hat{\mathbf{E}}_1\left(\mathbf{I} + \hat{\mathbf{Q}}_2\hat{\mathbf{G}}_1\right)^{-1}\hat{\mathbf{E}}_2 \tag{C2}$$

$$\hat{\mathbf{H}}_1 = \hat{\mathbf{F}}_2\left(\mathbf{I} + \hat{\mathbf{G}}_1\hat{\mathbf{Q}}_2\right)^{-1} \quad , \hat{\mathbf{L}}_1 = \hat{\mathbf{H}}_1\hat{\mathbf{G}}_1 \tag{C3}$$

$$\hat{\mathbf{L}}_2 = \hat{\mathbf{E}}_1\left(\mathbf{I} + \hat{\mathbf{Q}}_2\hat{\mathbf{G}}_1\right)^{-1} \quad , \hat{\mathbf{H}}_2 = \hat{\mathbf{L}}_2\hat{\mathbf{Q}}_2 \tag{C4}$$

Appendix D: the fixed Talbot approach (Abate and Valkó, 2004) to inverse Laplace transform

$$g(t,M) = \frac{\phi}{M}\left\{0.5\hat{g}(\phi)\exp(\phi t) + \sum_{\chi-1}^{M-1}\mathrm{Re}\left[\exp(ts(\psi_\chi))\hat{g}(s(\psi_\chi))(1 + \mathrm{i}\varrho(\psi_\chi))\right]\right\} \tag{D1}$$

$$\varrho(\psi) = \psi + (\psi\cot\psi - 1)\cot\psi \quad , s(\psi) = \phi\psi(1 + \cot\psi), \quad -\pi < \psi < \pi \tag{D2}$$

where $g(t,M)$ is the corresponding variable of $\hat{g}(s,M)$ in the physical domain, here $\phi = {}^{2M}/_{5t}$ and . M is the only one free parameter and stands for the number of terms to be summed. To control the rounding error in numerical computation of Eq. (D1), the accuracy requirement is: M = Decimal precision, and M = 10 in this study.

Appendix E: FRFT (Bailey and Swarztrauber, 1994) to inverse double Fourier transform

One dimensional Fourier transform inverse is firstly introduced,

$$y(x_k) = \mathrm{Y}^{-1}[\bar{y}(\xi),(-\xi_N,\xi_N)] = \omega\mathrm{e}^{-\mathrm{i}(\delta k^2 + \xi_N x_k)}\mathrm{D}_k^{-1}\{\mathrm{D}_j(l_j;2m)\mathrm{D}_j(\mathrm{D}_j(\delta,m);2m);2m\}$$

(E1)

$$l_j = \begin{cases} \overline{y}(\xi_j)\mathrm{e}^{-\mathrm{i}j(\omega\varphi+\delta j^2)}, & 0 \le j \le m-1 \\ 0, & m \le j \le 2m-1 \end{cases}$$

(E2)

$$z_j = \begin{cases} \mathrm{e}^{\mathrm{i}\delta j^2}, & 0 \le j \le m-1 \\ \mathrm{e}^{\mathrm{i}\delta(j-2m)^2}, & m \le j \le 2m-1 \end{cases}$$

(E3)

where $\mathrm{Y}^{-1}[\overline{y}(\xi),(-\xi_N,\xi_N)]$ is the Fourier transform inverse of $\overline{y}(\xi)$, $\xi_j = -\xi_N + \omega j$, $y(x_k)$ is the result at the discrete point x_k, here $x_k = \varphi + \gamma k$ $(0 \le k \le m-1)$, $\varphi = -0.5\gamma m$, γ and m are the spacing between adjacent discrete points and number of discrete segments in the physical domain, respectively. $\omega = 2\xi_N/m$ is the spacing between adjacent discrete points in the transform domain, ξ_N is the upper limit of integral transform and here $\xi_N = 16$. $\delta = 0.5\omega\gamma$. D_j and D_j^{-1} denote applying the fast Fourier transform to the vector and the corresponding inverse, respectively.

Based on Eq. (E1), one dimensional Fourier transform inverse can be realized, and the inversion of double Fourier transform can be further realized by repeating the above process.

References

Abate, J., and Valkó, P.P. 2004. Multi-precision Laplace transform inversion. *International Journal for Numerical Methods in Engineering*, 60(5): 979–993.

Adams, A.L., Germaine, J.T., Flemings, P.B., and Day-Stirrat, R.J. 2013. Stress induced permeability anisotropy of resedimented Boston Blue Clay. *Water Resources Research*, 49: 6561–6571.

Amaratunga, A., and Grozic, J.L.H. 2009. On the undrained unloading behaviour of gassy sands. *Canadian Geotechnical Journal*, 46(11): 1267–1276.

Ai, Z.Y., and Wang, L.J. 2016. Three-dimensional thermo-hydro-mechanical responses of stratified saturated porothermoelastic material. *Applied Mathematical Modelling*, 40: 8912–8933.

Arch, J., and Maltman, A. 1990. Anisotropic permeability and tortuosity in deformed wet sediments. *Journal of Geophysical Research*, 95: 9035–9045.

Bailey, D.H., and Swarztrauber, P.N. 1994. A fast method for the numerical evaluation of continuous Fourier and Laplace transforms. *SIAM Journal on Scientific Computing*, 15(5): 1105–1110.

Bear, J., and Cheng, A.H.-D. 2010. Modeling groundwater flow and contaminant transport. Springer, Dordrecht, Netherlands.

Biot, M.A. 1955. Theory of elasticity and consolidation for a porous anisotropic solid. *Journal of Applied Physics*, 26(2): 182–185.

Biot, M.A., and Willis, D.G. 1957. The elastic coefficients of the theory of consolidation. *Journal of Applied Physics*, 24: 594–601.

Bishop, A.W. 1959. The principle of effective stress. *Tekniske Ukeblad*, 39: 859–863.

Bishop, A.W. 1973. The influence of an undrained change in stress on the pore pressure in porous media of low compressibility. *Géotechnique*, 23(3): 435–442.

Black, D.K., and Lee, K.L. 1973. Saturating samples by back pressure. *Journal of the Soil Mechanics and Foundations Division*, 99: 75–93.

Borja, R.I., and Koliji, A. 2009. On the effective stress in unsaturated porous continua with double porosity. *Journal of the Mechanics and Physics of Solids*, 57: 1182–1193.

Carman, P.E. 1956. Flow of Gases through porous media, J Academic, New York.

Chang, C.S., and Duncan, J.M. 1983. Consolidation analysis for partly saturated clay by using an elastic-plastic effective stress-strain model. *International Journal for Numerical and Analytical Methods in Geomechanics*, 7: 39–55.

Chapuis, R.P., and Aubertin, M. 2003. On the use of the Kozeny Carman equation to predict the hydraulic conductivity of soils. *Canadian Geotechnical Journal*, 40(3): 616–628.

Chapuis, R.P. 2004. Predicting the saturated hydraulic conductivity of sand and gravel using effective diameter and void ratio. *Canadian Geotechnical Journal*, 41(5): 787–795.

Chen, G.J. 2004. Consolidation of multilayered half space with anisotropic permeability and compressible constituents. *International Journal of Solids and Structures*, 41(16-17): 4567–4586.

Cui, Y.J., Tinh Le, T., Tang, A.M., Delage, P., and Li, X.L. 2001. Investigating the time-dependent behaviour of Boom clay under thermo-mechanical loading. *Géotechnique*, 59(4): 319–329.

Deng, Y.F., Tang, A.M., Cui, Y.J., and Li, X-L. 2011. Study on the hydraulic conductivity of boom clay. *Canadian Geotechnical Journal*, 48: 1461–1470.

Faybishenko, B.A. 1995. Hydraulic behavior of quasi-saturated soils in the presence of entrapped air: laboratory experiments. *Water Resources Research*, 31(10): 2421–2435.

Fleischer, P., Orsi, T., Richardson, M., and Anderson, A. 2001. Distribution of free gas in marine sediments: a global overview. *Geo-Marine Letters*, 21(2): 103–122.

Fourie, A.B., Hofmann, B.A., Mikula, R.J., Lord, E.R.F., and Robertson, P.K. 2001. Partially saturated tailings sand below the phreatic surface. *Géotechnique*, 51(7): 577–585.

Fredlund, D.G. 1976. Density and compressibility characteristics of air-water mixtures. *Canadian Geotechnical Journal*, 13(4): 386–396.

Fredlund, D.G., and Rahardjo, H. 1993. Soil mechanics for unsaturated soils. John Wiley & Sons, Inc., New York.

Grozic, J.L.H., Robertson, P.K., and Morgenstern, N.R. 1999. The behavior of loose gassy sand. *Canadian Geotechnical Journal*, 36(3): 482–492.

Gray, W.G., and Schrefler, B.A. 2007. Analysis of the solid phase stress tensor in multiphase porous media. *International Journal for Numerical and Analytical Methods in Geomechanics*, 31: 541–581.

Hong, Y., Wang, L.Z., Ng, Charles W.W., and Yang, B. 2017. Effect of initial pore pressure on undrained shear behaviour of fine-grained gassy soil. *Canadian Geotechnical Journal*, 54(11): 1592–1600.

Hong, Y., Wang, X.T., Wang, L.Z., and Gao, Z.W. 2021. A state-dependent constitutive model for coarse-grained gassy soil and its application in slope instability modelling. *Computers and Geotechnics*, 129: 103847.

Hong, Y., Zhang, J.F., Wang, L.Z., and Liu, T. 2020. On evolving size and shape of gas bubble in marine clay under multi-stage loadings: microcomputed tomography (μCT) characterization and cavity contraction analysis. *Canadian Geotechnical Journal*, 57(7): 1072–1091.

Lade, P.V., and DE Boer, R. 1997. The concept of effective stress for soil, concrete and rock. *Géotechnique*, 47(1): 61–78.

Li, C.F., Cleall, P.J., Mao, J.F., and Muñoz-Criollo, J.J. 2018. Numerical simulation of ground source heat pump systems considering unsaturated soil properties and groundwater flow. *Applied Thermal Engineering*, 139: 307–316.

Liang, F.Y., Song, Z., and Jia, Y.J. 2017. Hydro-mechanical behaviors of the three-dimensional consolidation of multi-layered soils with compressible constituents. *Ocean Engineering*, 131: 272–281.

Mihalache, C., and Buscarnera, G. 2016. Controllability criteria for soils saturated by a compressible fluid. *Journal of Engineering Mechanics*, *ASCE*, 142(10): 04016076.

Mitchell, J.K., and Soga K. 2005. Fundamentals of Soil Behavior (3rd), John Wiley & Sons, Inc., New York.

Okusa, S. 1985. Wave-induced stresses in unsaturated submarine sediments. *Géotechnique*, 35(4): 517–532.

Pietruszczak, S., and Pande, G.N. 1996. Constitutive relations for partially saturated soils containing gas inclusions. *Journal of Geotechnical Engineering*, *ASCE*, 122(1): 50–59.

Rajapakse, R.K.N.D., and Senjuntichai, T. 1993. Fundamental solutions for a poroelastic half-space with compressible constituents. *Journal of Applied Mechanics*, 60(4): 844–856.

Rani, S., Kumar, R., and Singh, S.J. 2011. Consolidation of an anisotropic compressible poroelastic clay layer by axisymmetric surface loads. *International Journal of Geomechanics*, *ASCE*, 11(1): 65–71.

Rotta Loria, A.F., and Laloui, L. 2017. Thermally induced group effects among energy piles. *Géotechnique*, 67(5): 374–393.

Sakaguchi, A., Nishimura, T., and Kato, M. 2005. The effect of entrapped air on the quasisaturated soil hydraulic conductivity and comparison with the unsaturated hydraulic conductivity. *Vadose Zone Journal*, 4(1): 139–144.

Sanzeni, A., Colleselli, F., and Grazioli, D. 2013. Specific surface and hydraulic conductivity of fine-grained soils. *Journal of Geotechnical and Geoenvironmental Engineering*, *ASCE*, 139: 1828–1832.

Savvidou, C., and Booker, J.R. 1988. Consolidation around a spherical heat source with a decaying power output. *Computers and Geotechnics*, 5(3): 227–244.

Savvidou, C., and Booker, J.R. 1991. Consolidation of a deep homogeneous clay stratum subjected to a surface temperature change. *Proceedings of the Ninth Asian Regional Conference on Soil Mechanics and Foundation Engineering*, Bangkok: Southeast Asian Geotechnical Society: 425–428.

Schiffman, R.L. 1970. The stress components of a porous medium. *Journal of Geophysical Research*, 75: 4035–4038.

Scholes, O.N., Clayton, S.A., Hoadley, A.F.A., and Tiu, C. 2007. Permeability anisotropy due to consolidation of compressible porous media. *Transport in Porous Media*, 68(3): 365–387.

Selvadurai, A.P.S., and Suvorov, A.P. 2014. Thermo-poromechanics of a fluid-filled cavity in a fluid-saturated geomaterial. *Proceedings of The Royal Society A Mathematical Physical and Engineering Sciences*, 470: 20130634.

Selvadurai, A.P.S., and Najari, M. 2017. The thermo-hydro-mechanical behavior of the argillaceous Cobourg Limestone. *Journal of Geophysical Research: Solid Earth*, 122: 4157–4171.

Sills, G.C., and Wheeler, S.J. 1992. The significance of gas for offshore operations. *Continental Shelf Research*, 12(10): 1239–1250.

Sills, G.C., Wheeler, S.J., Thomas, S.D., and Gardner, T.N. 1991. Behaviour of offshore soils containing gas bubbles. *Géotechnique*, 41(2): 227–241.

Skempton, A.W. 1960. Effective stress in soils, concrete and rock. *Conference on Pore Pressure and Suction in Soils*, Butterworths, 4–6.

Sneddon, IN. 1972. The use of integral transform. McGraw-Hill Company, New York.

Suklje, L. 1969. Rheological aspects of soil mechanics. *Wiley Interscience*, New York, 123.

Sultan, N., Delage, P., and Cui, Y.J. 2002. Temperature effects on the volume change behaviour of Boom clay. *Engineering Geology*, 64(2-3): 135–145.

Sultan, N., De Gennaro, V., and Puech, A. 2012. Mechanical behaviour of gas-charged marine plastic sediments. *Géotechnique*, 62(9): 751–766.

Sultan, N., and Garziglia, S. 2014. Mechanical behaviour of gas-charged fine sediments: model formulation and calibration. *Géotechnique*, 64(11): 851–864.

Tarantino, A. 2013. Basic concepts in the mechanics and hydraulics of unsaturated geomaterials, in mechanics of unsaturated geomaterials, Wiley, Hoboken.

Terzaghi, K. 1936. The shearing resistance of saturated soils and the angle between the planes of

shear. *First International Conference on Soil Mechanics*, Harvard University, I, 54–56.

Terzaghi, K. 1945. Stress conditions for the failure of saturated concrete and rock. *Proceedings-American Society for Testing Materials*, 45: 777–801.

Thomas, H.R., Cleall, P.J., Dixon, D., and Mitchell, H.P. 2009. The coupled thermal-hydraulic-mechanical behaviour of a large scale in-situ heating experiment. *Géotechnique*, 59(4): 401–413.

Verruijt, A. 2018. Numerical and analytical solutions of poroelastic problems. *Geotechnical Research*, 5(1): 39–50.

Waite, W.F; Santamarina, J.C; Cortes, D.D; Dugan, B; Espinoza, D.N., Germaine, J., Jang, J., Jung, J.W., Kneafsey, T.J., Shin, H., Soga, K., Winters, W.J., and Yun, T.S. 2009. Physical properties of hydrate-bearing sediments. *Reviews of Geophysics*, 47(4): RG4003.

Wang, L.J., and Ai, Z.Y. 2018. Quasi–static thermal analyses of layered compressible poroelastic materials with a finite depth or half-space. *Applied Mathematical Modelling*, 59: 272–292.

Wang, L.J., Zhu, B, Chen, Y.M., Chen, R.P., and Shi, X.S. 2019a. Precise model for predicting excess pore-water pressure of layered soils induced by thermal-mechanical loads. *Journal of Engineering Mechanics, ASCE*, 145(1): 04018114.

Wang, L.J., Zhu, B, Chen, Y.M., Kong, D.Q., and Chen, R.P. 2019b. Coupled consolidation and heat flow analysis of layered soils surrounding cylindrical heat sources using a precise integration technique. *International Journal for Numerical and Analytical Methods in Geomechanics*, 43: 1539–1561.

Wongsaroj, J., Soga, K., and Mair, R.J. 2013. Tunnelling-induced consolidation settlements in London Clay. *Géotechnique*, 63(13): 1103–1115.

Yue, Z.Q., Selvadurai, A.P.S., and Law, K.T. 1994. Excess pore pressure in a poroelastic seabed saturated with a compressible fluid. *Canadian Geotechnical Journal*, 31: 989–1003.

Zhong, W.X. 2004. On precise integration method. *Journal of Computational and Applied Mathematics*, 163(1): 59–78.

Zhong, W.X., Lin, J.H., and Gao, Q. 2004. The precise computation for wave propagation in stratified materials. *International Journal for Numerical Methods in Engineering*, 60(1): 11–25.

Zhu, B., Ye, Z.G., Wang, L.J., Kong, D.Q., Xu, W.J., Kolditz, O., Nagel, T., and Chen, Y.M. 2020. Hydro-mechanical behavior of unsaturated soil surrounding a heated pipeline considering moisture evaporation and condensation. *Computers and Geotechnics*, 119: 103377.

Table 1 Expressions of the coefficient *b* for quasi-saturated or saturated soils

b	Note	References
1	-	Terzaghi, 1936; Skempton, 1960; Chen, 2004; Deng *et al*, 2011 and many others
n	n = porosity	Terzaghi, 1945; Biot, 1955; Schiffman, 1970
$1-a_c$	a_c = grain contact area per unit area of plane	Bishop, 1959; Lade and De Bore, 1997
$1-\frac{C_{sg}}{C_{ssk}}$	C_{sg} = compressibility of soil grain, C_{ssk} = compressibility of soil skeleton	Biot and Willis, 1957; Bishop, 1973; Lade and De Bore, 1997; Gray and Schrefler, 2007
$1-\frac{C_{ssk}}{C_s}$	C_s = compressibility of soil as a whole	Black and Lee, 1973; Liang *et al*, 2017; Verruijt, 2018
$1-(1-n)\frac{C_{sg}}{C_s}$	-	Suklje, 1969; Chapuis, 2004; Lade and De Bore, 1997

Table 2 Selected parameter values for parametric investigation

Parameter	Default values	Other values
Thermal expansion characteristic of soil grain, β_l/β_s	1000	1, 2, 5, 10
Initial degree of saturation, S_{rini}	99.999%	99.0%, 97.5%, 95.0%, 92.5%, 90.0%
Degree of saturation varied with temperature, Eq. (11d)	Yes	No
Anisotropic permeability, c_h/c_v	1	0.1, 10, 50, 100

List of figures

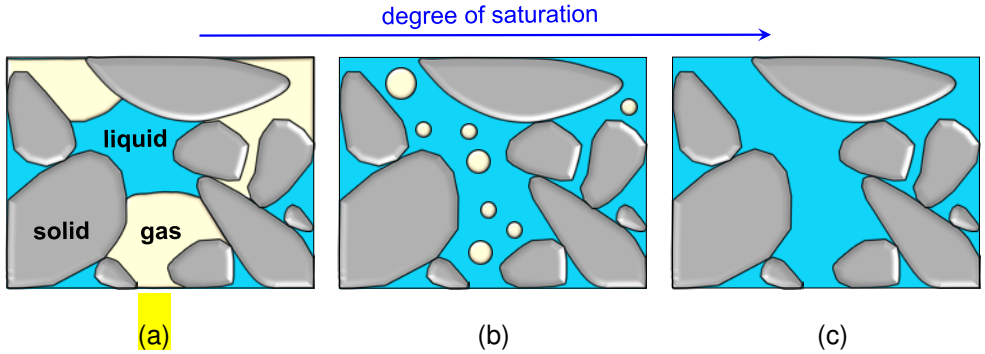

Fig. 1 Schematic diagram of soils with different degree of saturation: (a) unsaturated soil with gas phase continuity; (b) quasi-saturated soil with occluded bubbles; (c) fully saturated soil.

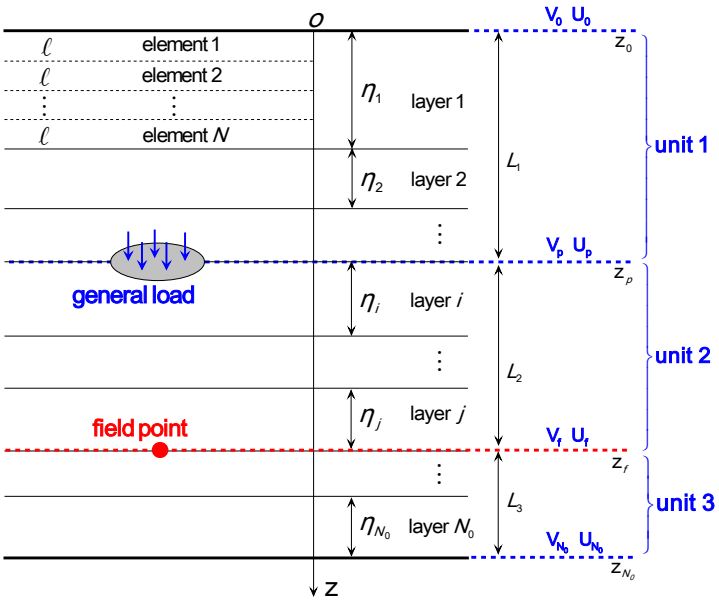

Fig. 2 Three unit division diagram of layered system containing N_0 natural layers

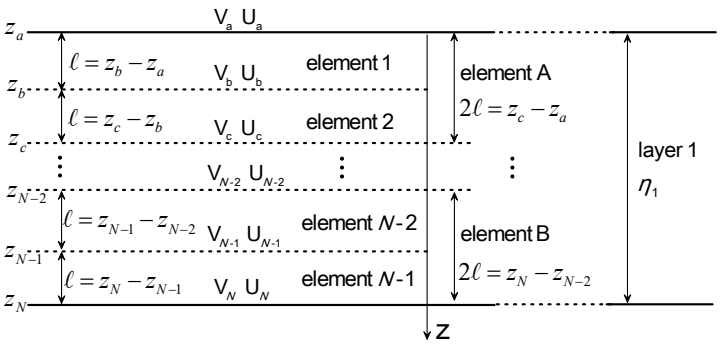

Fig. 3 Combination diagram of adjacent layer-elements

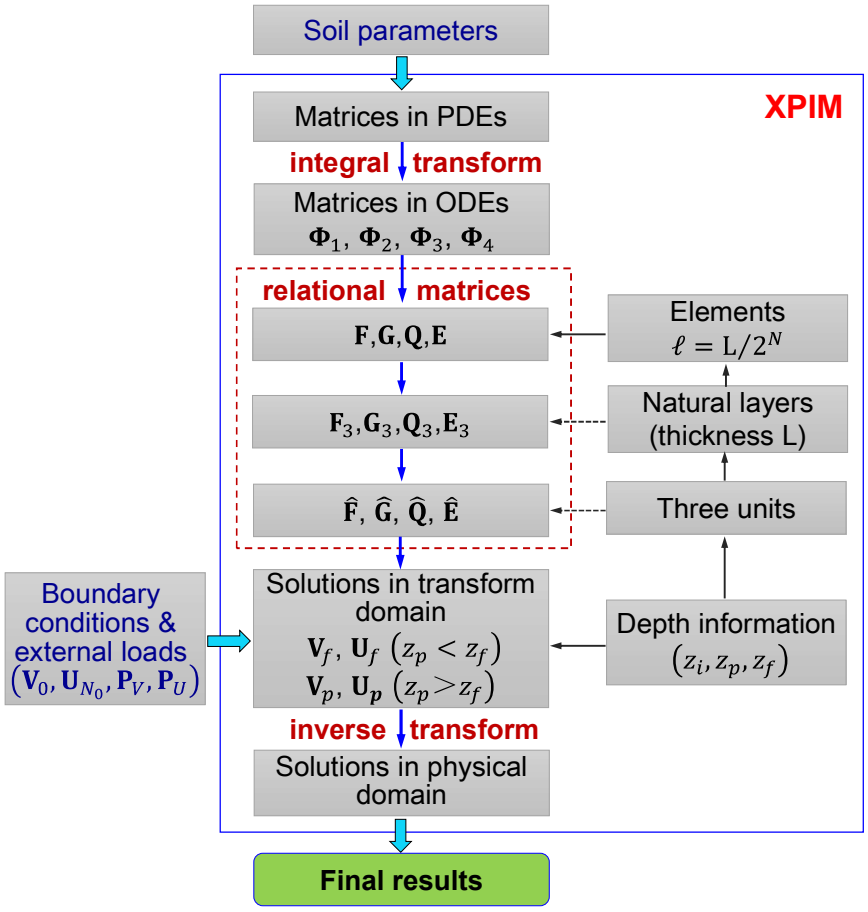

Fig. 4 Overall scheme of the XPIM

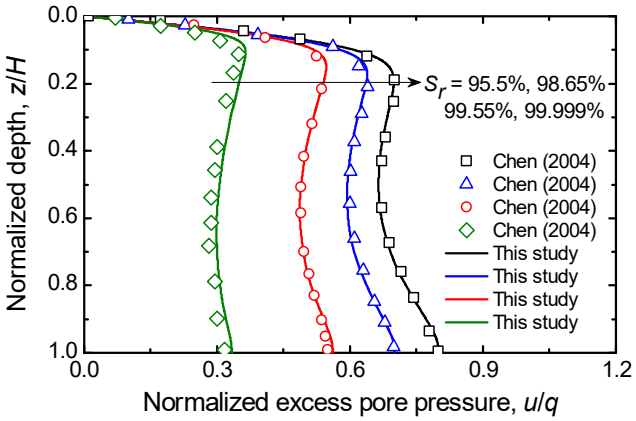

15

16 Fig. 5 Comparisons of EPP at τ = 0.001 with different initial S_r along the central line subject

17 to a surface load

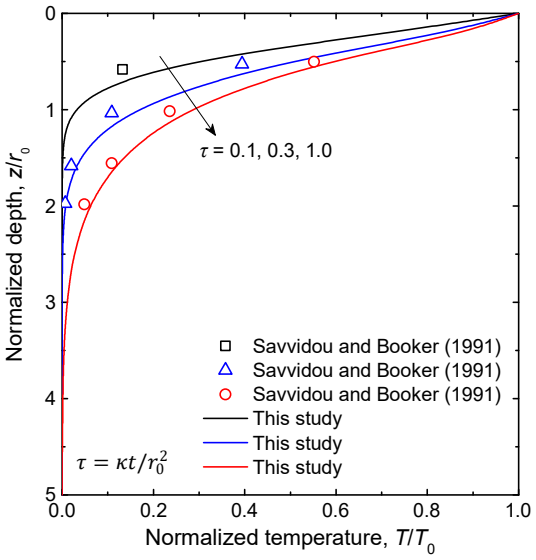

(a)

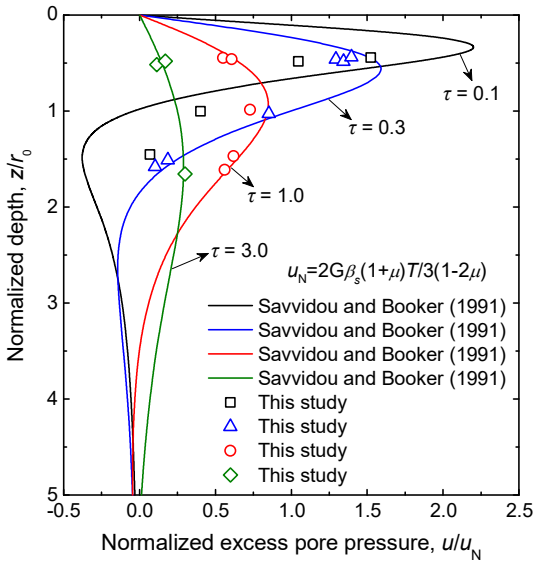

(b)

Fig. 6 Comparison of the present solutions with test results subjected to surface temperature change at a range of time factors (τ): (a) temperature variation; (b) EPP.

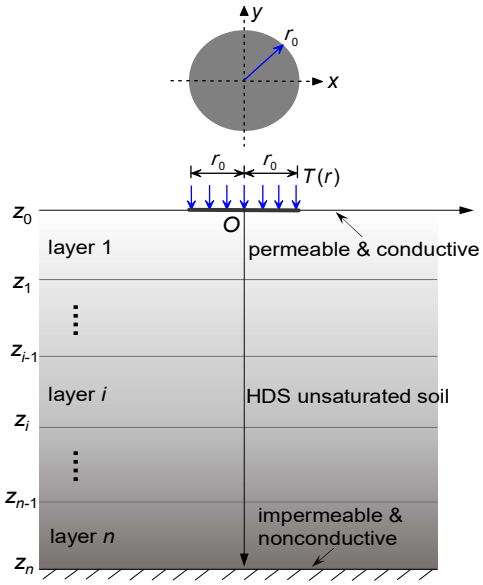

Fig. 7 Diagram of the HDS unsaturated soil applied with a surface temperature change $T(r)$

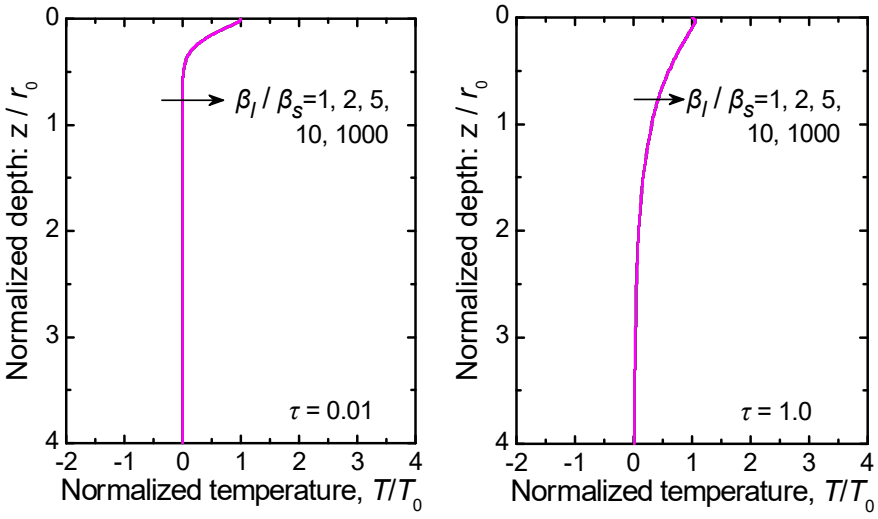

(a) (b)

Fig. 8 Effects of thermal expansion characteristics of soil grains on temperature variation: (a) $\tau = 0.01$; (b) $\tau = 1.0$.

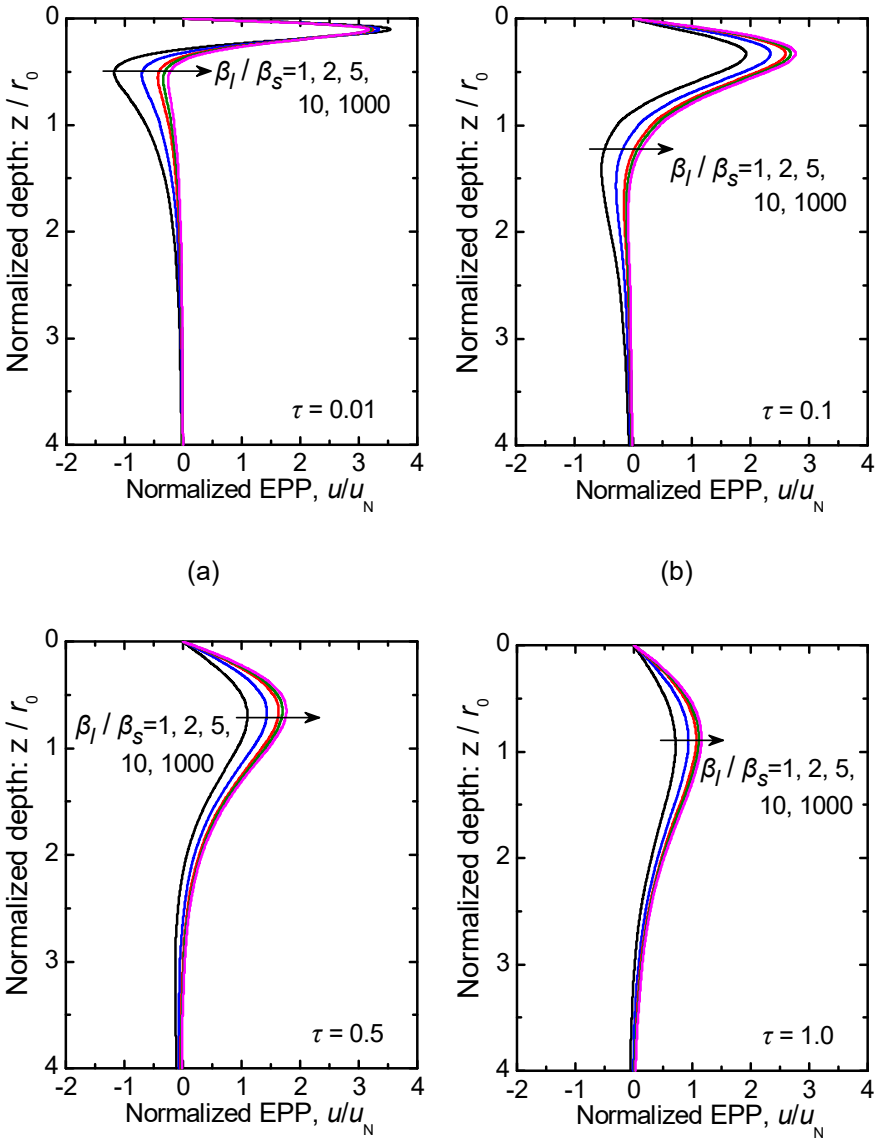

Fig. 9 Effects of thermal expansion characteristics of soil grains on EPP: (a) $\tau = 0.01$; (b) $\tau = 0.1$; (c) $\tau = 0.5$; (d) $\tau = 1.0$.

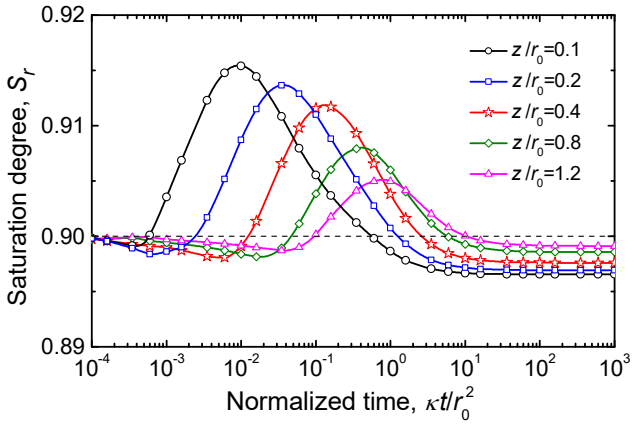

(a)

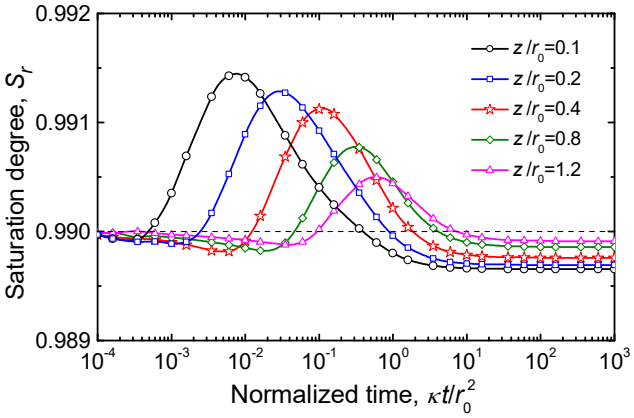

(b)

Fig. 10 Time-dependent development of S_r at different depth subjected to temperature change: (a) S_{rini} = 90%; (b) S_{rini} = 99%.

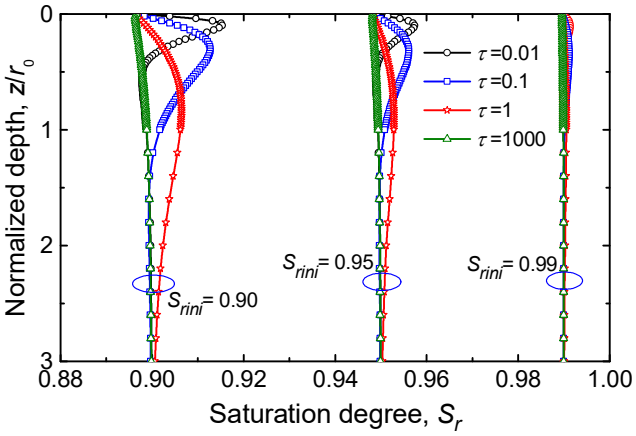

42

43 Fig. 11 Variation of S_r with depth for different S_{rini}

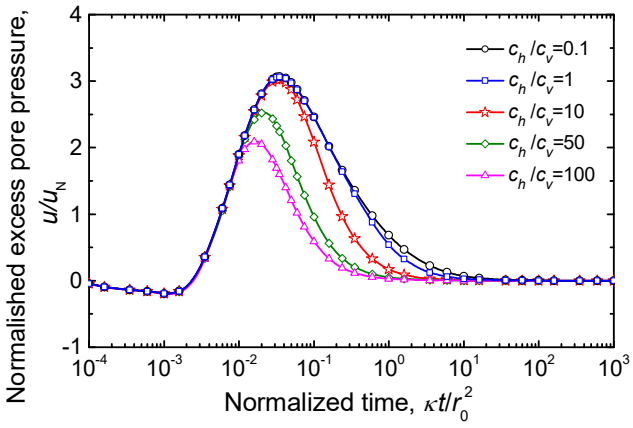

(a)

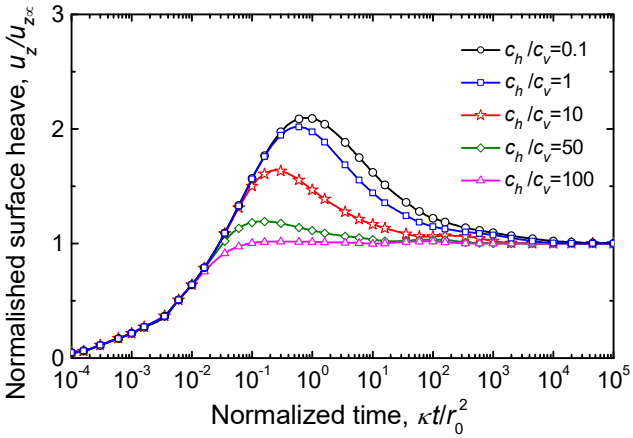

(b)

Fig. 12 Effect of anisotropic permeability c_h/c_v on time-dependent behaviour (S_r = 95%): (a) EPP; (b) Vertical surface displacement.

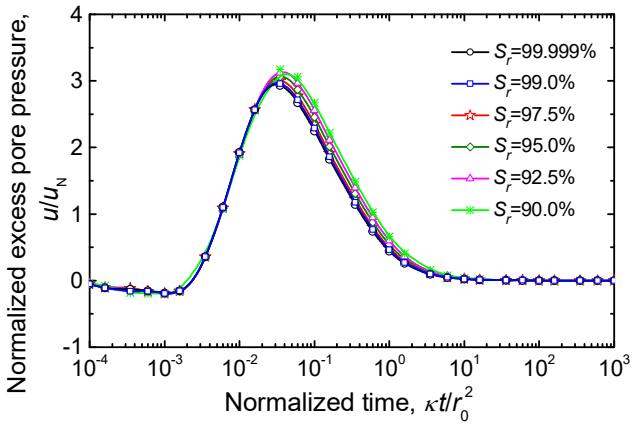

(a)

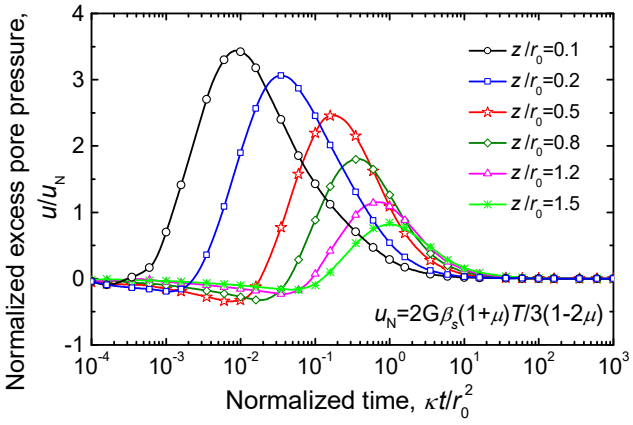

(b)

Fig. 13 Time-dependent development of EPP: (a) with different S_r at depth of z/r_0=0.2; (b) at different depth (S_r = 95%).

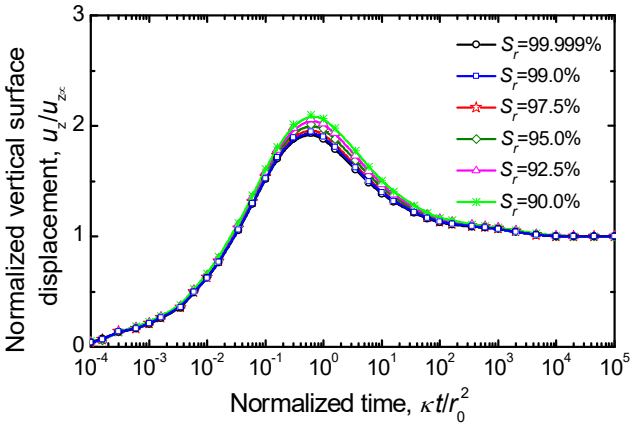

56

57 (a)

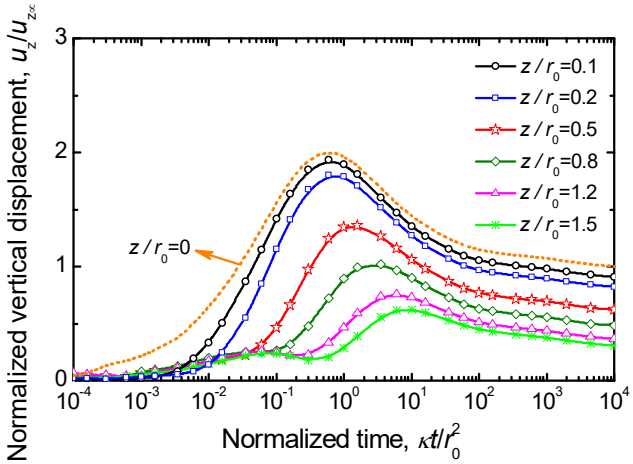

58

59 (b)

60 Fig. 14 Time-dependent development of vertical displacement: (a) with different initial S_r; (b)

61 at different depth (S_r = 95%).